

## NUMERICAL MODELING OF FLUID FLOW AND TIME-LAPSE SEISMOGRAMS APPLIED TO CO<sub>2</sub> STORAGE AND MONITORING

G. B. Savioli<sup>1</sup>, J. E. Santos<sup>2</sup>, J. M. Carcione<sup>3</sup>, D. Gei<sup>3</sup>

<sup>1</sup> Laboratorio de Ingeniería de Reservorios, Instituto del Gas y del Petróleo - Facultad de Ingeniería, Universidad de Buenos Aires (gsavioli@fi.uba.ar)

<sup>2</sup> CONICET, Inst. del Gas y del Petróleo Fac. Ingeniería, Universidad de Buenos Aires  
Universidad Nacional de La Plata  
Department of Mathematics, Purdue University, U.S.A (santos@math.purdue.edu)

<sup>3</sup> Istituto Nazionale di Oceanografia e di Geofisica Sperimentale (OGS), Borgo Grotta Gigante 42c, 34010 Sgonico, Trieste, Italy (jcarcione@inogs.it)

**Abstract.** *CO<sub>2</sub> sequestration in the underground is a valid alternative approach for mitigating the greenhouse effect. Nevertheless, very little is known about the effectiveness of CO<sub>2</sub> storage over very long periods. In this work we introduce a methodology to model the gas flow and monitor the storage. For this purpose, we integrate numerical simulators of CO<sub>2</sub>-brine flow and seismic wave propagation. The simultaneous flow of brine and CO<sub>2</sub> is modeled with the Black-Oil formulation for two-phase flow in porous media, using PVT data as a simplified thermodynamic model. Wave propagation is based on an equivalent viscoelastic model that considers dispersion and attenuation effects. Densities and bulk and shear moduli are assumed to be dependent on pressure and saturation. The spatial pressure and CO<sub>2</sub> saturation distributions computed with the flow simulator are used to determine the phase velocities and attenuation coefficients of the P and S waves from White's model. Numerical examples of CO<sub>2</sub> injection and time-lapse seismograms are analyzed. The proposed methodology is able to identify the spatio-temporal distribution of CO<sub>2</sub> after its injection, and constitutes an important tool to monitor the CO<sub>2</sub> plume and analyze storage integrity, providing an early warning in case should any leakage may occur.*

**Keywords:** *CO<sub>2</sub> Sequestration, black-oil model, viscoelastic model*

### 1. INTRODUCTION

Geologic storage of CO<sub>2</sub> consists in injecting the gas into a geologic formation at depths typically greater than 1000 m, where it is present at supercritical conditions [1]. Saline aquifers are suitable as storage sites due to their large volume and their common occurrence in nature. Numerical modeling of CO<sub>2</sub> injection and seismic monitoring are important tools

to understand the behavior of CO<sub>2</sub> after its injection and make long term predictions. The CO<sub>2</sub> injection operation at the Sleipner gas field in the North Sea, operated by Statoil and the Sleipner partners, is the world first industrial scale CO<sub>2</sub> injection project designed specifically as a greenhouse gas mitigation measure [10]. Time-lapse seismic surveys aim to demonstrate storage integrity. In recent works [16] [9], seismic modeling has been used to monitor the spatio-temporal distribution of CO<sub>2</sub> using synthetic generated CO<sub>2</sub> saturation fields. Instead, in this work we introduce a methodology to model the gas flow and monitor the storage. For this purpose, we integrate numerical simulators of CO<sub>2</sub>-brine flow and seismic wave propagation. The simultaneous flow of brine and CO<sub>2</sub> is modeled with the Black-Oil formulation for two-phase flow in porous media [2].

Wave propagation is based on an equivalent viscoelastic model that considers dispersion and attenuation effects. In regions with partial CO<sub>2</sub> saturation, following White's theory [19], we consider P-wave attenuation due to wave-induced fluid flow at mesoscopic scales using a model of porous layers alternately saturated with brine and CO<sub>2</sub>. The results of the flow simulator are used to compute the phase velocities and attenuation coefficients of P and S waves from White's model. Numerical examples of CO<sub>2</sub> injection and time-lapse seismograms in the Utsira Sand aquifer at Sleipner field are analyzed. We build a petrophysical model of the Utsira formation based on fractal porosity and clay content and taking into account the variation of properties with pore pressure and CO<sub>2</sub> saturation. This model is able to simulate embedded mudstone layers of very low permeability that accumulate CO<sub>2</sub> but also allow its migration. The proposed methodology is able to identify the spatio-temporal distribution of CO<sub>2</sub> after its injection. Attenuation and dispersion effects are clearly observed in the snapshots and the recorded traces. This methodology is able to identify the horizontal and vertical saturation distribution of CO<sub>2</sub> over long periods of time.

## 2. THE BLACK-OIL FORMULATION OF TWO-PHASE FLOW IN POROUS MEDIA

The simultaneous flow of brine and CO<sub>2</sub> in porous media is described by the well-known Black-Oil formulation applied to two-phase, two component fluid flow [2]. We represent the brine (subindex *b*) by the oil phase and the CO<sub>2</sub> (subindex CO2) by the gas phase. In this way, CO<sub>2</sub> component may dissolve in the brine phase but the brine is not allowed to vaporize into the CO<sub>2</sub> phase. The differential equations are obtained by combining the mass conservation equations with Darcy's empirical law.

The mass conservation equations are:

- For the CO<sub>2</sub> component,

$$-\nabla \cdot (\rho_{CO_2} \hat{v}_{CO_2} + C_{CO_2,b} \rho_b \hat{v}_b) + q_{CO_2} = \frac{\partial [\phi (\rho_{CO_2} S_{CO_2} + C_{CO_2,b} \rho_b S_b)]}{\partial t}, \quad (1)$$

- For the brine component,

$$-\nabla \cdot (C_{b,b} \rho_b \hat{v}_b) + q_b = \frac{\partial [\phi (C_{b,b} \rho_b S_b)]}{\partial t}, \quad (2)$$

where  $\rho$  is density,  $\hat{v}$  is Darcy velocity,  $S$  is saturation,  $q$  mass rate of injection per unit volume and  $\phi$  is porosity.  $C_{CO_2,b}$ ,  $C_{b,b}$  are the mass fractions of  $CO_2$  and brine in the brine phase, respectively. In the Black-Oil formulation these fractions are computed using a simplified thermodynamic model (PVT data), as

$$C_{CO_2,b} = \frac{R_s \rho_{CO_2} B_{CO_2}}{B_b \rho_b} \quad (3)$$

$$C_{b,b} = \frac{\rho_b^{SC}}{B_b \rho_b} \quad (4)$$

where  $R_s$ ,  $B_{CO_2}$  and  $B_b$  are PVT data, defined as

- $R_s = \frac{V_{dCO_2}^{SC}}{V_b^{SC}}$ ,  $CO_2$  solubility in brine;
- $B_{CO_2} = \frac{V_{CO_2}^{res}}{V_{CO_2}^{SC}}$ ,  $CO_2$  formation volume factor;
- $B_b = \frac{(V_{dCO_2}^{res} + V_b^{res})}{V_b^{SC}}$ , brine formation volume factor;

with  $V_{CO_2}^{res}$ ,  $V_b^{res}$  and  $V_{dCO_2}^{res}$  the volume of  $CO_2$ , brine and dissolved  $CO_2$  in brine at reservoir conditions; and  $V_{CO_2}^{SC}$ ,  $V_b^{SC}$  and  $V_{dCO_2}^{SC}$  are the volume of  $CO_2$ , brine and dissolved  $CO_2$  in brine at standard conditions, respectively. Also,  $\rho_b^{SC}$  and  $\rho_{CO_2}^{SC}$  are the  $CO_2$  and brine densities at standard conditions.

The empirical Darcy's Law gives the momentum balance for the fluids,

$$\hat{v}_{CO_2} = -\frac{\kappa}{\eta_{CO_2}} \frac{k_{rCO_2}}{\eta_{CO_2}} (\nabla p_{CO_2} - \rho_{CO_2} g \nabla D), \quad (5)$$

$$\hat{v}_b = -\frac{\kappa}{\eta_b} \frac{k_{rb}}{\eta_b} (\nabla p_b - \rho_b g \nabla D), \quad (6)$$

where  $p_{CO_2}$ ,  $p_b$  are the fluid pressures and  $\kappa$  is the absolute permeability tensor. Also, for  $\beta = CO_2, b$ , the functions  $k_{r\beta}$  and  $\eta_\beta$  are the relative permeability and viscosity of the  $\beta$ -phase, respectively.

Replacing (3)-(6) in (1)-(2) and dividing by  $\rho_{CO_2}^{SC}$  and  $\rho_b^{SC}$ , the following nonlinear system of partial differential equation is obtained,

$$\begin{aligned} \nabla \cdot \left( \frac{\kappa}{B_{CO_2} \eta_{CO_2}} \frac{k_{rCO_2}}{\eta_{CO_2}} (\nabla p_{CO_2} - \rho_{CO_2} g \nabla D) + \frac{R_s \kappa}{B_b \eta_b} \frac{k_{rb}}{\eta_b} (\nabla p_b - \rho_b g \nabla D) \right) + \frac{q_{CO_2}}{\rho_{CO_2}^{SC}} \\ = \frac{\partial \left[ \phi \left( \frac{S_{CO_2}}{B_{CO_2}} + \frac{R_s S_b}{B_b} \right) \right]}{\partial t}, \end{aligned} \quad (7)$$

$$\nabla \cdot \left( \frac{\kappa}{B_b \eta_b} \frac{k_{rb}}{\eta_b} (\nabla p_b - \rho_b g \nabla D) \right) + \frac{q_b}{\rho_b^{SC}} = \frac{\partial \left[ \phi \frac{S_b}{B_b} \right]}{\partial t}. \quad (8)$$

Two algebraic equations relating the saturations and pressures complete the system:

$$S_b + S_{CO_2} = 1, \quad p_{CO_2} - p_b = P_C(S_b), \quad (9)$$

where  $P_C$  is the capillary pressure.

The unknowns for the Black-Oil model are the fluid pressures  $p_{CO_2}, p_b$  and the saturations  $S_{CO_2}, S_b$  for the  $CO_2$  and brine phases.

$R_s$  and  $B_b$  can be expressed in terms of the equilibrium properties obtained from an equation of state [14]:

- $R_s = \frac{\tilde{\rho}_b^{SC} \chi_{CO_2}}{\tilde{\rho}_{CO_2}^{SC} (1 - \chi_{CO_2})}$
- $B_b = \frac{\rho_b^{SC}}{\rho_b (1 - \omega_{CO_2})}$

where  $\tilde{\rho}_b^{SC}$  and  $\tilde{\rho}_{CO_2}^{SC}$  are the brine and  $CO_2$  molar density at standard conditions; and  $\chi_{CO_2}$  and  $\omega_{CO_2}$  are the  $CO_2$  mole fraction and the  $CO_2$  mass fraction in the brine phase. This conversion from compositional data from equations of state into the black-oil PVT data is performed applying an algorithm developed by Hassanzadeh et al [14],

The numerical solution was obtained employing the public domain software BOAST [12]. BOAST solves the differential equations using IMPES (IMPLICIT Pressure EXPLICIT Saturation), a semi-implicit finite difference technique [17].

### 3. A VISCOELASTIC MODEL FOR WAVE PROPAGATION

The propagation of waves in porous media is described using an equivalent viscoelastic model that takes into account the dispersion and attenuation effects due to the presence of heterogeneities in the fluid and solid phase properties.

The equation of motion in a 2D isotropic viscoelastic domain  $\Omega$  with boundary  $\partial\Omega$  can be stated in the space-frequency domain as

$$-\omega^2 \rho u - \nabla \cdot \sigma(u) = f(x, \omega), \quad \Omega \quad (10)$$

$$-\sigma(u)\nu = i\omega \mathcal{D}u, \quad \partial\Omega, \quad (11)$$

where  $u = (u_x, u_y)$  is the displacement vector. Here  $\rho$  is the bulk density and (11) is a first-order absorbing boundary condition using the positive definite matrix  $\mathcal{D}$ .

The stress tensor  $\sigma(u)$  is defined in the space-frequency domain by

$$\sigma_{jk}(u) = \lambda_G(\omega) \nabla \cdot u \delta_{jk} + 2\mu_m(\omega) \varepsilon_{jk}(u), \quad \Omega, \quad (12)$$

where  $\varepsilon_{jk}(u)$  denotes the strain tensor and  $\delta_{jk}$  is the Kronecker delta.

The coefficient  $\mu_m$  in (12) is the shear modulus of the dry matrix, while the Lamé coefficient is  $\lambda_G = K_G - \frac{2}{3}\mu_m$  in 3D and  $\lambda_G = K_G - \mu_m$  in 2D.  $K_G$  is the Gassmann's

undrained bulk modulus, computed as follows [5]:

$$\begin{aligned} K_G &= K_m + \alpha^2 M \\ \alpha &= 1 - \frac{K_m}{K_s}, \\ M &= \left[ \frac{\alpha - \phi}{K_s} + \frac{\phi}{K_f} \right]^{-1}. \end{aligned}$$

where

- $K_m$ : bulk modulus of the dry matrix
- $K_s$ : bulk modulus of the solid grains
- $K_f$ : bulk modulus of the saturant fluid

To introduce viscoelasticity we use the *correspondence principle* stated by M. Biot [3],[4], i.e. we replace the real poroelastic coefficients in the constitutive relations by complex frequency dependent poroviscoelastic moduli satisfying the same relations as in the elastic case, with some necessary thermodynamic restrictions.

In this work we use the linear viscoelastic model presented in [13] to make the undrained bulk modulus  $K_G$  and the shear modulus  $\mu_m$  complex and frequency dependent. Thus, we take

$$K_G(\omega) = \frac{K_G^{re}}{R_{K_G}(\omega) - iT_{K_G}(\omega)}, \quad \mu_m(\omega) = \frac{\mu_m^{re}}{R_{\mu_m}(\omega) - iT_{\mu_m}(\omega)}, \quad (13)$$

where  $\omega = 2\pi f$ : angular frequency and  $K_G^{re}, \mu_m^{re}$  are the relaxed Gassmann's and shear modulus.

The functions  $R_l$  and  $T_l$ ,  $l = K_G, \mu_m$ , associated with a continuous spectrum of relaxation times, characterize the viscoelastic behaviour and are given by [13]

$$R_l(\omega) = 1 - \frac{1}{\pi \widehat{Q}_l} \ln \frac{1 + \omega^2 T_{1,l}^2}{1 + \omega^2 T_{2,l}^2}, \quad T_l(\omega) = \frac{2}{\pi \widehat{Q}_l} \tan^{-1} \frac{\omega(T_{1,l} - T_{2,l})}{1 + \omega^2 T_{1,l} T_{2,l}}.$$

The model parameters  $\widehat{Q}_l$ ,  $T_{1,l}$  and  $T_{2,l}$  are taken such that the quality factors  $Q_l(\omega) = T_l/R_l$  are approximately equal to  $\widehat{Q}_l$  in the range of frequencies where the equations are solved, which makes this model convenient for geophysical applications.

The approximate solution of (10) with the boundary conditions (11) is obtained using a finite element procedure employing a uniform partition  $\mathcal{T}^h$  of the computational domain  $\Omega$  into square subdomains  $\Omega_m$ ,  $m = 1, \dots, L$  of side length  $h$ . To approximate each component of the solid displacement vector we employed the nonconforming finite element space, since it generates less numerical dispersion than the standard bilinear elements [11], [21]. It can be demonstrated that the error associated with this numerical procedure measured in the energy norm is of order  $h$ .

## 4. THE ITERATIVE DOMAIN DECOMPOSITION ALGORITHM

### 4.1. Weak Formulation

We proceed to formulate the variational form for viscoelastic waves: Find  $\widehat{u} \in [H^1(\Omega)]^N$  such that

$$-(\rho\omega^2\widehat{u}, \varphi) + \sum_{pq} (\tau_{pq}(\widehat{u}), \varepsilon_{pq}(\varphi)) + i\omega \langle \mathcal{A}\widehat{u}, \varphi \rangle_{\Gamma} = (\widehat{f}, \varphi), \quad \varphi \in [H^1(\Omega)]^N.$$

Here  $(f, g) = \int_{\Omega} f \bar{g} dx$  and  $\langle f, \bar{g} \rangle = \int_{\Gamma} f \bar{g} d\Gamma$  denote the complex  $[L^2(\Omega)]^N$  and  $[L^2(\Gamma)]^N$  inner products. Also,  $H^1(\Omega)$  denotes the usual Sobolev space of functions in  $L^2(\Omega)$  with first derivatives in  $L^2(\Omega)$ .

### 4.2. Finite Element Method

The nonconforming finite element space used in this paper was first described in [9]. For  $h > 0$ , let  $\mathcal{T}_h$  be a quasiregular partition of  $\overline{\Omega}$  such that  $\overline{\Omega} = \cup_{j=1}^J \overline{\Omega}_j$  with  $\Omega_j$  being  $N$ -rectangles of diameter bounded by  $h$ . Set  $\Gamma_j = \partial\Omega \cap \partial\Omega_j$  and  $\Gamma_{jk} = \Gamma_{kj} = \partial\Omega_j \cap \partial\Omega_k$ , we denote by  $\xi_j$  and  $\xi_{jk}$  the centroids of  $\Gamma_j$  and  $\Gamma_{jk}$ , respectively.

We consider a nonconforming finite element space constructed using the following reference rectangular element

$$\widehat{R} = [-1, 1]^2 \quad S_2(\widehat{R}) = \text{Span} \left\{ \frac{1}{4} \pm \frac{1}{2}x - \frac{3}{8} \left( (x^2 - \frac{5}{3}x^4) - (y^2 - \frac{5}{3}y^4) \right), \right. \\ \left. \frac{1}{4} \pm \frac{1}{2}y + \frac{3}{8} \left( (x^2 - \frac{5}{3}x^4) - (y^2 - \frac{5}{3}y^4) \right) \right\}.$$

The four degrees of freedom associated with  $S_2(\widehat{R})$  are the values at the mid points of the faces of  $\widehat{R}$ , i.e., the values at the nodal points  $a_1 = (-1, 0)$ ,  $a_2 = (0, -1)$ ,  $a_3 = (1, 0)$  and  $a_4 = (0, 1)$ . For example the basis function  $\psi_1(x, y) = \frac{1}{4} - \frac{1}{2}x - \frac{3}{8} \left( (x^2 - \frac{5}{3}x^4) - (y^2 - \frac{5}{3}y^4) \right)$  is such that  $\psi_1(a_1) = 1$  and  $\psi_1(a_j) = 0$ ,  $j = 2, 3, 4$ .

One of the main advantages of using nonconforming elements to solve wave propagation phenomena is that the amount of information exchanged among processors in a domain decomposition iterative procedure is considerable reduced as compared to the case when conforming elements are employed. Another property of the nonconforming elements is that it is possible to obtain an estimate on the speed of convergence of the iterative domain decomposition procedure as a function of the mesh size  $h$ .

Set  $NC_j^h = S_N(\Omega_j)$ ,  $N = 2, 3$  and define a nonconforming finite element space in the following manner

$$NC^h = \left\{ v \mid v_j := v|_{\Omega_j} \in NC_j^h, j = 1, \dots, J; \quad v_j(\xi_{jk}) = v_k(\xi_{jk}), \forall \{j, k\} \right\}.$$

The global nonconforming Galerkin procedure is defined as follows: find  $\widehat{u}^h \in [NC^h]^2$  such that

$$-(\rho\omega^2\widehat{u}^h, \varphi) + \sum_{pq} (\tau_{pq}(\widehat{u}^h), \varepsilon_{pq}(\varphi)) + i\omega \langle \mathcal{A}\widehat{u}^h, \varphi \rangle_{\Gamma} = (\widehat{f}, \varphi), \quad \varphi \in [NC^h]^2.$$

Next, we will define a discrete domain decomposition iterative hybridized procedure. For this purpose, we introduce a new set  $\tilde{\Lambda}^h$  of Lagrange multipliers  $\lambda_{jk}^h$  associated with the stress values  $-\tau(\hat{u}_j)\nu_{jk}(\xi_{jk})$ :

$$\tilde{\Lambda}^h = \{\lambda^h : \lambda^h|_{\Gamma_{jk}} = \lambda_{jk}^h \in [P_0(\Gamma_{jk})]^N = [\Lambda_{jk}^h]^N\}.$$

Then, given an initial guess  $(\hat{u}_j^{h,0}, \lambda_{jk}^{h,0}, \lambda_{kj}^{h,0}) \in [NC_j^h]^N \times [\Lambda_{jk}^h]^N \times [\Lambda_{kj}^h]^N$ , compute  $(\hat{u}_j^{h,n}, \lambda_{jk}^{h,n}) \in [NC_j^h]^N \times [\Lambda_{jk}^h]^N$  as the solution of the equations

$$\begin{aligned} & -(\rho\omega^2\hat{u}_j^{h,n}, \varphi)_j + \sum_{pq} (\tau_{pq}(\hat{u}^{h,n}), \varepsilon_{pq}(\varphi))_j + i\omega \left\langle \left\langle \mathcal{A}\hat{u}_j^{h,n}, \varphi \right\rangle \right\rangle_{\Gamma_j} \\ & + \sum_k \left\langle \left\langle \lambda_{jk}^{h,n}, \varphi \right\rangle \right\rangle_{\Gamma_{jk}} = (\hat{f}, \varphi)_j, \quad \varphi \in [NC_j^h]^N, \end{aligned} \quad (14)$$

$$\lambda_{jk}^{h,n} = -\lambda_{kj}^{h,n-1} + i\beta_{jk}[\hat{u}_j^{h,n}(\xi_{jk}) - \hat{u}_k^{h,n-1}(\xi_{jk})], \quad \text{on } \Gamma_{jk}. \quad (15)$$

It can be shown that

$$[\hat{u}^{h,n} - \hat{u}^h]^2 \rightarrow 0 \text{ in } [L^2(\Omega)]^2 \quad \text{when } n \rightarrow \infty,$$

so that in the limit the global nonconforming Galerkin approximation is obtained [13].

## 5. PETROPHYSICAL MODEL

The petrophysical model assumes a shaly sand and is generated from the initial porosity  $\phi_0$  (at hydrostatic pore pressure  $p_H$ ) and clay content  $C$ . We model fractal variations of  $\phi_0$  and  $C$ .

The pressure dependence of properties is based on the following relationship between porosity and pore pressure  $p$ ,

$$\frac{(1 - \phi_c)}{K_s}(p - p_H) = \phi_0 - \phi + \phi_c \ln \frac{\phi}{\phi_0}, \quad (16)$$

where  $\phi_c$  is a critical porosity.

The bulk modulus of the dry matrix is estimated from the pressure dependent porosity using the Krief equation [9],

$$K_m = K_s(1 - \phi)^{A/(1-\phi)}, \quad (17)$$

where the bulk modulus of the solid grains  $K_s$  is the arithmetic average of the Hashin Shtrikman upper and lower bounds. The rock is formed with quartz (bulk modulus of 40 GPa) and clay (bulk modulus of 15 GPa).

We assume the grain to be a Poisson medium, then the shear modulus of the solid grains is  $\mu_s = 3K_s/5$  and we set

$$\mu_m = \mu_s(1 - \phi)^{A/(1-\phi)}. \quad (18)$$

The black-oil simulator needs the compressibility  $C_{pp}$  defined by Zimmerman et al. [20], which is given by

$$C_{pp} = \frac{1}{\phi} \left( \frac{1}{K_m} - \frac{1 + \phi}{K_s} \right) \quad (19)$$

As permeability is anisotropic, we consider horizontal permeability  $\kappa_x$  and vertical permeability  $\kappa_z$ . Carcione et al. [7] derived a model depending on porosity and clay content, assuming that a shaly sandstone is composed of a sandy matrix and a shaly matrix with partial permeabilities

$$\kappa_q = \frac{R_q^2 \phi^3}{45(1 - \phi)^2(1 - C)} \quad \text{and} \quad \kappa_c = \frac{R_c^2 \phi^3}{45(1 - \phi)^2 C} \quad (20)$$

where  $R_q$  and  $R_c$  denote the average radii of sand and clay particles, respectively.

Therefore, the average permeability of the shaly sandstone along the horizontal direction is given by

$$\frac{1}{\kappa_z} = \frac{1 - C}{\kappa_q} + \frac{C}{\kappa_c} \quad (21)$$

Following Carcione et al. [8], we assume

$$\frac{\kappa_x}{\kappa_z} = \frac{1 - (1 - 0.3a) \sin \pi S_w}{a(1 - 0.5 \sin \pi S_w)}, \quad (22)$$

where  $a$  is a permeability-anisotropy parameter and  $S_w$  is the brine saturation.

Note that for  $S_w = 0$  or  $1$ ,  $\kappa_z = a\kappa_x$ . It is  $\kappa_x > \kappa_z$  at full water saturation, due to pore cross sections which are larger in the  $x$ -direction.

As water saturation is reduced, and the larger pores drained first, a saturation is reached at which  $\kappa_x = \kappa_z$ . Then, as saturation is further reduced,  $\kappa_x < \kappa_z$ . At the other end (full gas saturation), we have again  $\kappa_x > \kappa_z$ .

## 6. NUMERICAL EXPERIMENTS

### 6.1. Idealized model of the Utsira formation

To test the proposed methodology, we consider an idealized model of the Utsira formation. It has 300 m thickness (top at 800 m and bottom 1100 m b.s.l.). Within the formation, there are two mudstone layers of 4 m thickness located at 860 m and 1010 m.

The pressure-temperature conditions are  $T = 31.7z + 3.4$ , where  $T$  is the temperature (in degrees Celsius) and  $z$  is the depth (in km b.s.l.);  $p_H = \rho_w g z$  is the hydrostatic pressure, with  $\rho_w = 1040 \text{ kg/m}^3$  the density of brine and  $g$  the constant gravity. In the Utsira sandstone,  $\rho = (1 - \phi)\rho_s + \phi\rho_f$ , where  $\phi(z)$  is the porosity,  $\rho_s$  is the grain density and  $\rho_f$  is the fluid density. The Utsira grain density is  $\rho_s = 2550 \text{ kg/m}^3$  (both quartz and clay), while  $\rho_f = (1 - S_w)\rho_g + S_w\rho_w$ , where  $S_w$  is the water saturation and  $\rho_g$  is the  $\text{CO}_2$  density, which is obtained from the Peng-Robinson equations as a function of  $T$  and  $p$ , where  $p$  is the pore pressure [9].



We define  $\phi_0 = \phi(p_H)$  fractal for the Utsira, with an average value of 37% and a variation of  $\pm 3\%$ . In the mudstone layers  $\phi_0 = 24\%$  constant. In the same way, the clay content is estimated as  $C = 5\%$  for the Utsira, with a fractal variation of 5% and  $C = 85\%$  (uniform) for the mudstone layers. The initial porosity distribution and clay content are shown in Figure 1.

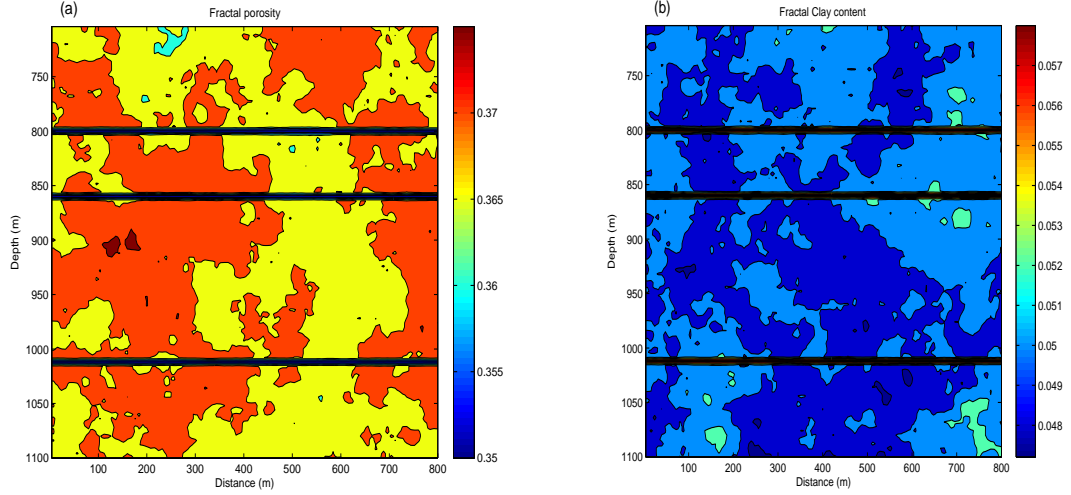


Figure 1. (a) Initial porosity and (b) clay content fractal distributions

Then we include the porosity variation as function of pressure (eq. (16)). Figure 2 shows the resulting initial porosity and compressibility distribution (eq. (19)).

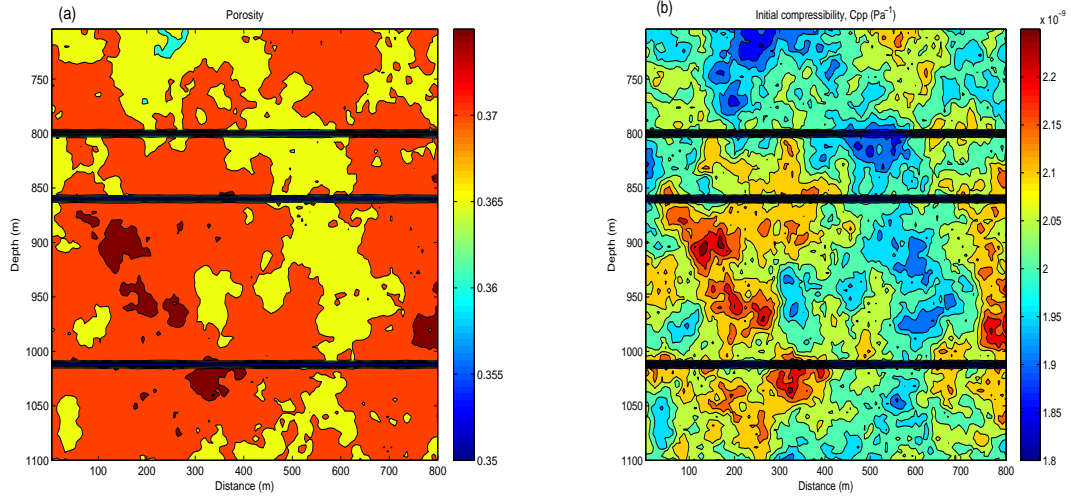


Figure 2. (a) Porosity and (b) compressibility distributions

Horizontal and vertical permeability distributions computed with eqs. (21), (22) can be seen in Figure 3. Initially, as  $S_w = 1$ , vertical permeability is a fraction of horizontal permeability.

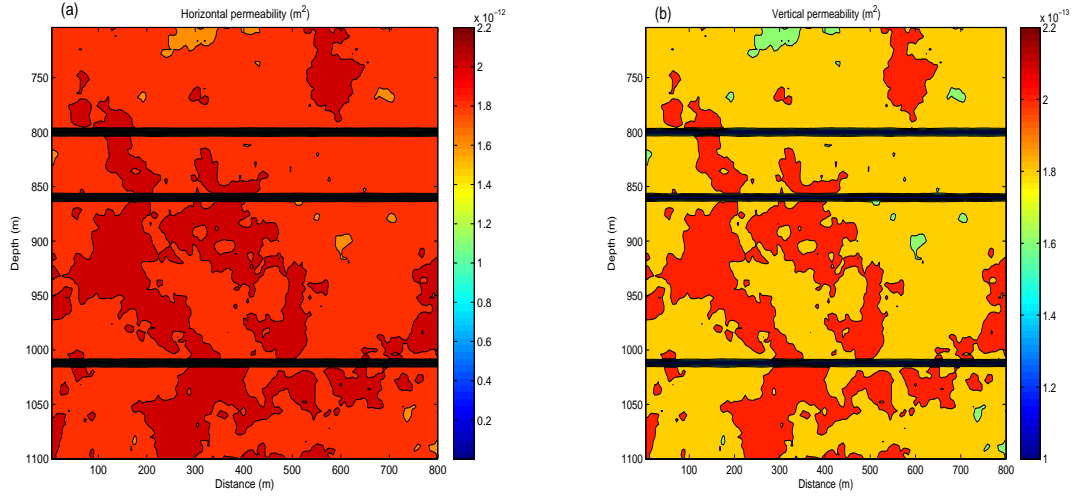


Figure 3. (a) Horizontal and (b) vertical permeability distributions

We consider wave propagation in this poroelastic medium. The bulk modulus and the shear modulus of the dry matrix for the initial pressure are shown in Figure 4.

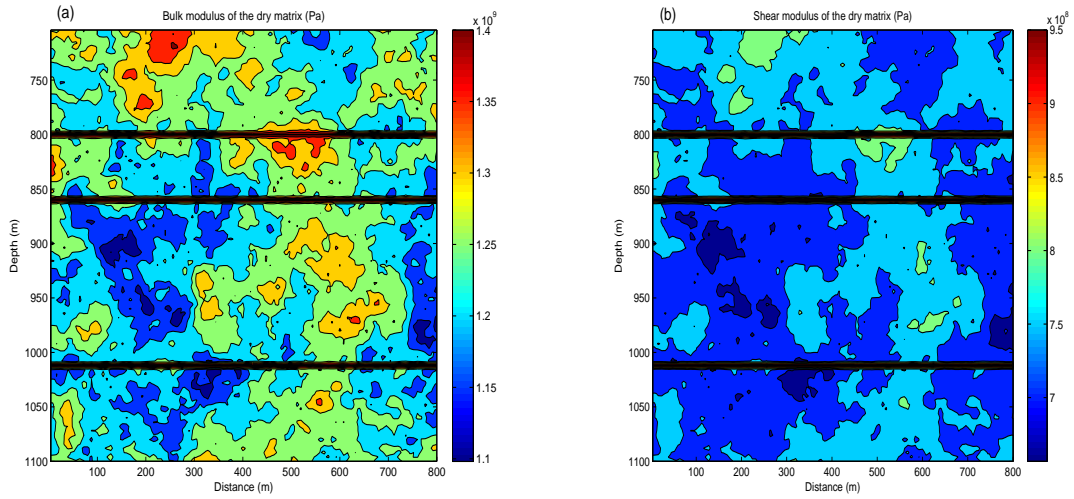


Figure 4. (a) Bulk modulus and (b) shear modulus of the dry matrix

It is convenient first to approximate a saturated porous medium  $\Omega$  by a viscoelastic solid and use the concept of complex velocity as follows. Recall that in a viscoelastic solid, the quality factor  $Q(\omega)$  is defined by the relation

$$Q(\omega) = \frac{\text{Re}(v_P^2)}{\text{Im}(v_P^2)},$$

where  $v_P$  is the complex compressional velocity given by

$$v_P(\omega) = \sqrt{\frac{E}{\rho_b}}. \quad (23)$$

In (23)  $\bar{\rho}_b$  is the average bulk density over  $\Omega$  and  $E = E(\omega) = |E|e^{i\theta}$  is the complex plane wave modulus associated with the domain  $\Omega$  as defined by White et al [19]. The quality factor is related to the loss angle  $\theta$  by the formula

$$Q^{-1}(\omega) = \tan \theta.$$

The source function  $f$  is a compressional point source located inside the region at  $x = 400$  m,  $z = 710$  m. The iterative procedure was used to find the time Fourier transforms of the displacement vectors of the solid and fluid phases for 100 equally spaced temporal frequencies in the interval  $[0, 60\text{Hz}]$ .

## 6.2. Injection Modeling

CO<sub>2</sub> is injected at a constant flow rate of 5000 SCF/d. The injection point is located at the bottom of the Utsira formation:  $x = 400$  m,  $z = 1060$  m. Results are computed applying the BOAST simulator. The evolution of CO<sub>2</sub> saturation distribution is illustrated in Figure 5 which shows CO<sub>2</sub> saturation after 1 year, 5 years and 10 years of CO<sub>2</sub> injection. In the left column the results are obtained without considering variation of properties as function of pressure and saturation. On the other hand, in the right column, the results are computed updating the properties every two years. It can be observed that after one year of injection there is a CO<sub>2</sub> accumulation below the bottom mudstone layer. But this layer is not sealed, it has a very low permeability so, as time increases, part of the injected fluid migrates through it. Therefore, at 5 years, another CO<sub>2</sub> accumulation appears below the mudstone layer located at 860 m. After 10 years of injection, there are 3 zones of CO<sub>2</sub> accumulation: below the lower and upper mudstone layers and below the top of the Utsira formation. The accumulation is more important when the variation of properties is taken into account. The reason of this behavior is the increment of vertical permeability as CO<sub>2</sub> saturation increases, following equation (22). The vertical permeability variation is illustrated in Figure 6.

Figure 7 displays the distribution of P-wave phase velocity after 10 years of CO<sub>2</sub> injection and Figure 8 the vertical profile of the P-wave phase velocity corresponding to  $x = 200$  m. The velocity changes due to the presence of the mudstone layers and CO<sub>2</sub> accumulation are clearly observed.

### 6.2.1 Seismic Monitoring

The objective of this section is to analyze the capability of seismic monitoring to identify zones of CO<sub>2</sub> accumulation. With this purpose, the media is excited with the point source located at  $x = 400$  m,  $z = 710$  m.

Time histories measured near the surface are shown in Figure 9, before CO<sub>2</sub> injection (a) and after 10 years of CO<sub>2</sub> injection (b). The upper reflection in both figures is due to the direct wave coming from the point source. Two other reflections appear: the lower is generated by the CO<sub>2</sub> accumulations below the mudstone layer at depth  $z = 1010$  m, the third reflection (the upper one) is due to the accumulation below the upper mudstone layer.

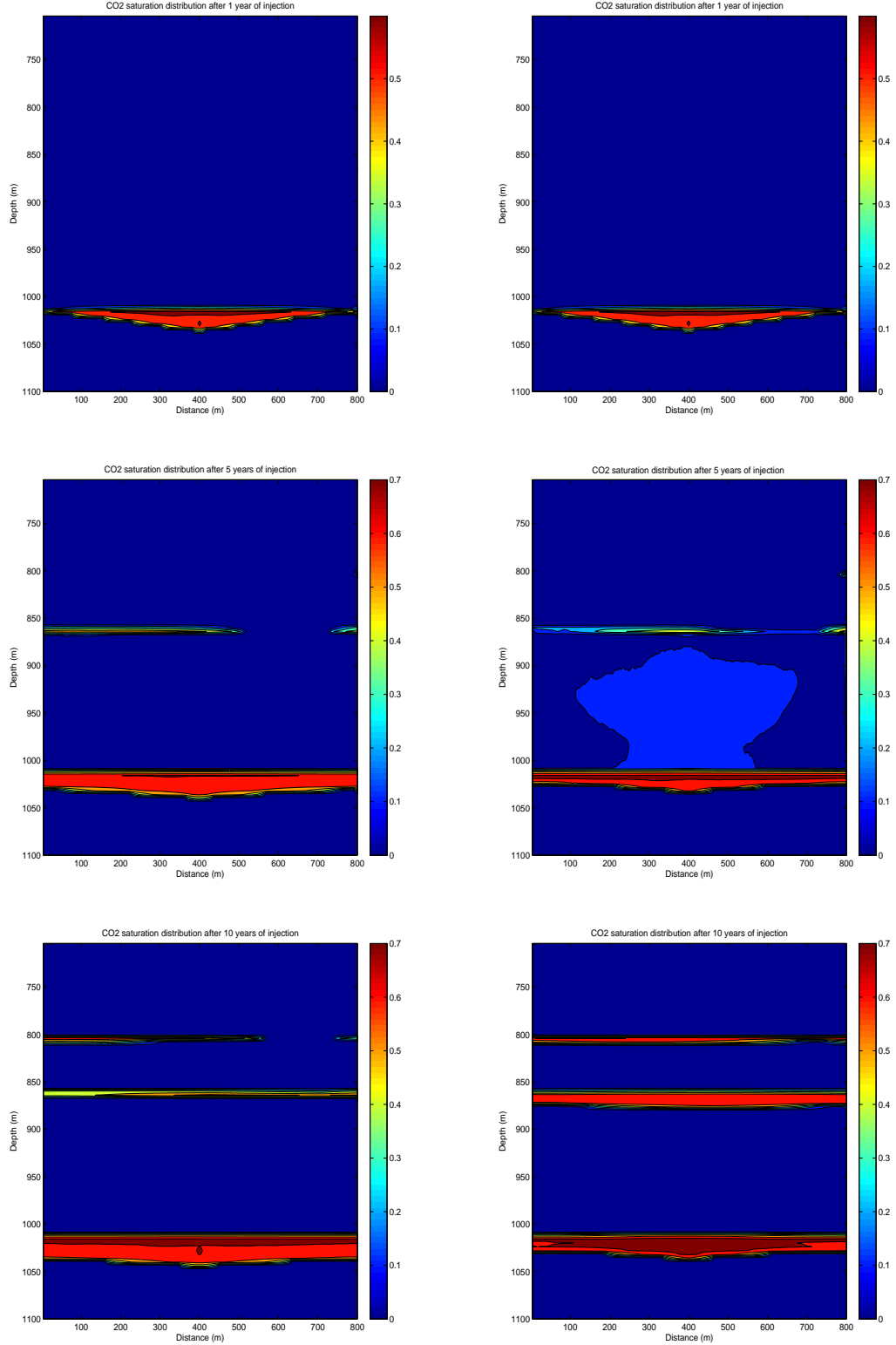


Figure 5. CO<sub>2</sub> saturation distribution after 1, 5 and 10 years of CO<sub>2</sub> injection, disregarding (left) or considering (right) variation of properties

## 7. CONCLUSIONS

In this work we integrate numerical simulators of CO<sub>2</sub>-brine flow and seismic wave propagation to model and monitor CO<sub>2</sub> storage in saline aquifers. We also build a petrophysi-

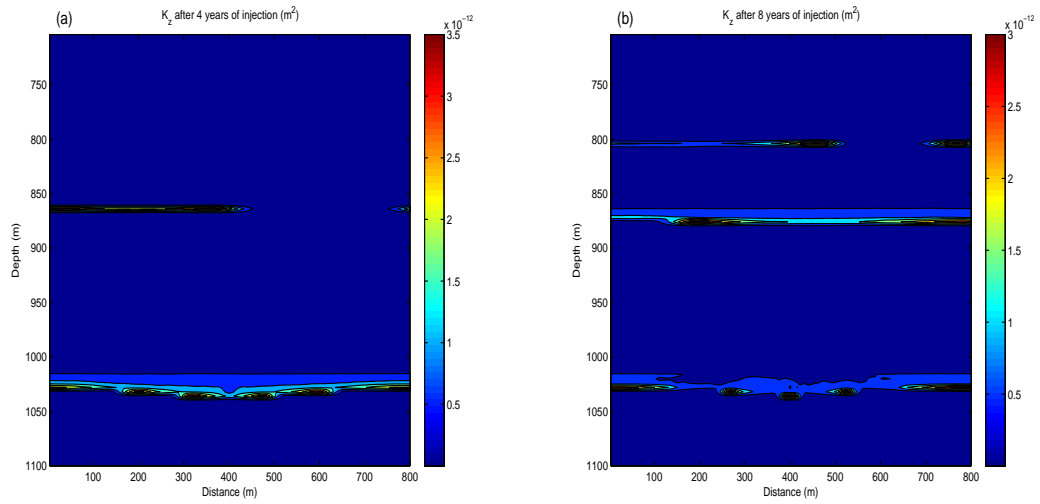


Figure 6. Vertical permeability distribution after 4 years (a) and 8 years (b) of CO<sub>2</sub> injection

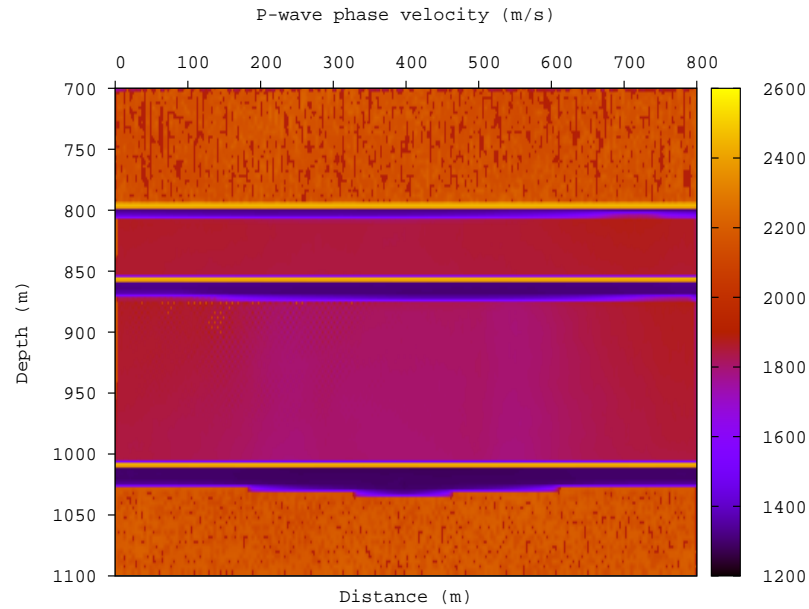


Figure 7. P-wave phase velocity after 10 years of CO<sub>2</sub> injection

cal model of a shaly sandstone based on fractal porosity and clay content and considering the variation of properties with pore pressure and fluid saturation. Numerical examples show the effectiveness of this methodology to detect the spatio-temporal distribution of CO<sub>2</sub>. Therefore, it constitutes an important tool to monitor the migration and dispersal of the CO<sub>2</sub> plume and to make long term predictions.

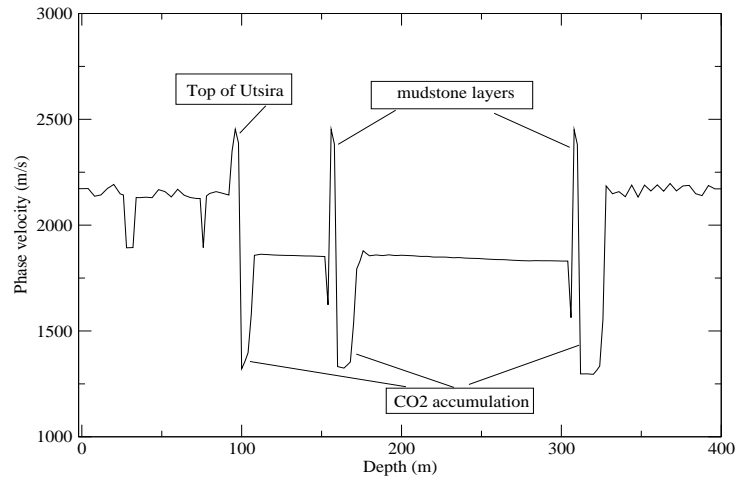


Figure 8. Vertical profile of the P-wave phase velocity after 10 years of CO<sub>2</sub> injection

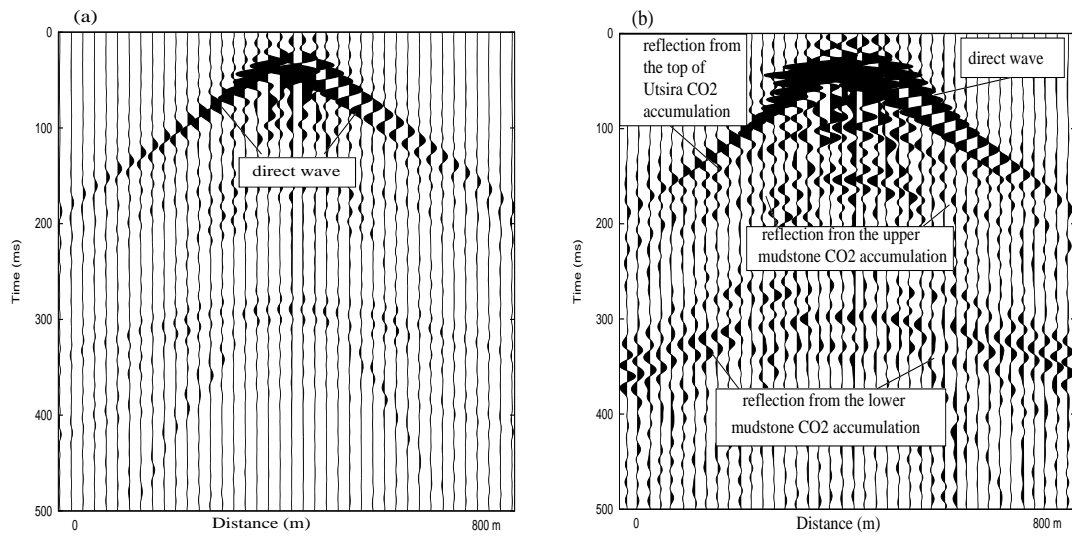


Figure 9. Time histories measured near the surface before (a) and after 10 years of CO<sub>2</sub> injection (b)

## 8. REFERENCES

- [1] Arts R., Chadwick A., Eiken O., Thibeu S., Nooner S., "Ten years of experience of monitoring CO<sub>2</sub> injection in the utsira sand at sleipner, offshore Norway". *First break* 26, 65-72, 2008.
- [2] Aziz K., Settari A., "Petroleum Reservoir Simulation". *Elsevier Applied Science Publishers*, Great Britain, 1985.

- [3] Biot M.A., "Theory of deformation of a porous viscoelastic anisotropic solid". *J. Appl. Phys.* 27, 459-467, 1956.
- [4] Biot M.A., "Mechanics of deformation and acoustic propagation in porous media". *J. Appl. Phys.* 33, 1482-1498, 1962.
- [5] Carcione, J. M., "Wave Fields in Real Media. Theory and numerical simulation of wave propagation in anisotropic, anelastic, porous and electromagnetic media". *Elsevier* (Second edition, extended and revised), 2007.
- [6] Carcione J.M., Picotti S., "P-wave seismic attenuation by slow-wave diffusion: Effects of inhomogeneous rock properties". *Geophysics* 71(3), O1-O8, 2006.
- [7] Carcione J.M., Gurevich, B., Cavallini, F., "A generalized Biot-Gassmann model for the acoustic properties of shaley sandstones". *Geophys. Prosp.* 48, 539-557, 2000.
- [8] Carcione J.M., Helbig K., Helle, H. B., "Effects of pressure and saturating fluid on wave velocity and attenuation of anisotropic rocks". *Int.J. Rock Mech. Min. Sci.* 40, 389-403, 2003.
- [9] Carcione J.M., Picotti S., Gei D., Rossi G., "Physics and seismic modeling for monitoring CO<sub>2</sub> storage". *Pure and Applied Geophysics* 163, 175-207, 2006.
- [10] Chadwick A., Arts R., Eiken O., "4d seismic quantification of a growing CO<sub>2</sub> plume at sleipner, North Sea". *Dore A G and Vincent B (Eds) Petroleum Geology: North West Europe and Global Perspectives - Proc. 6th Petroleum Geology Conference*, 1385-1399, 2005.
- [11] Douglas, Jr. J., Santos J.E., Sheen D., Ye X., "Nonconforming Galerkin methods based on quadrilateral elements for second order elliptic problems". *RAIRO Mathematical Modelling and Numerical Analysis (M2AN)* 33, 747-770, 1999.
- [12] Fanchi J., "Principles of Applied Reservoir Simulation". *Gulf Professional Publishing Company*, Houston, Texas, 1997.
- [13] Ha T., Santos J.E., Sheen D., "Nonconforming finite element methods for the simulation of waves in viscoelastic solids". *Comput. Meth. Appl. Mech. Engrg.* 191, 5647-5670, 2002.
- [14] Hassanzadeh H., Pooladi-Darvish M., Elsharkawy A., Keith D., Leonenko Y., "Predicting PVT data for CO<sub>2</sub>-brine mixtures for black-oil simulation of CO<sub>2</sub> geological storage". *International Journal of Greenhouse Gas Control* 2, 65-77, 2008.
- [15] Liu H.P., Anderson D.L., Kanamori H., "Velocity dispersion due to anelasticity; implications for seismology and mantle composition". *Geophys. J. R. Astr. Soc.* 147, 41-58, 1976.
- [16] Santos J.E., Rubino J.G., Ravazzoli C.L., "Modeling mesoscopic attenuation in a highly heterogeneous biot's medium employing an equivalent viscoelastic model". *Proc. 78th Annual International Meeting SEG (Las Vegas)* 2212-2215, 2008.
- [17] Savioli G., Bidner M.S., "Simulation of the oil and gas flow toward a well - a stability analysis". *Journal of Petroleum Science and Engineering* 48, 53-69, 2005.
- [18] Spycher N., Pruess K., "CO<sub>2</sub>-H<sub>2</sub>O mixtures in the geological sequestration of CO<sub>2</sub>. ii. partitioning in chloride brines at 12-100 c and up to 600 bar". *Geochim. Cosmochim. Acta* 69 13, 3309-3320, 2005.
- [19] White J.E., Mikhaylova N.G., Lyakhovitskiy F.M., "Low-frequency seismic waves in fluid-saturated layered rocks". *Izvestija Academy of Sciences USSR, Physics of Solid Earth* 10, 654-659, 1975.
- [20] Zimmerman R. W., Somerton W. H., King, M. S., "Compressibility of Porous Rocks". In *Journal of Geophysical Research* 91, 12765-12777, 1986.
- [21] Zyserman F.I., Gauzellino P.M., Santos J.E., "Dispersion analysis of a non-conforming finite element method for the Helmholtz and elastodynamic equations". *Int. J. Numer. Meth. Engng.* 58, 1381-1395, 2003.